IOP Publishing Phys. Med. Biol. 67 (2022) 225013 https://doi.org/10.1088/1361-6560/ac9e40

Physics in Medicine & Biology

IPEM Institute of Physics and Engineering in Medicine

RECEIVED
30 August 2022

REVISED
12 October 2022

ACCEPTED FOR PUBLICATION
27 October 2022

PUBLISHED
16 November 2022

PAPER

Theory of sleep/wake cycles affecting brain elastography

Gary R Ge[1], Wei Song[2], Maiken Nedergaard[2], Jannick P Rolland[1] and Kevin J Parker[3]

[1] Institute of Optics, University of Rochester, 480 Intercampus Drive, Box 270186, Rochester, NY 14627, United States of America
[2] Center for Translational Neuromedicine, University of Rochester Medical Center, 601 Elmwood Avenue, Box 645, Rochester, NY 14642, United States of America
[3] Department of Electrical and Computer Engineering, University of Rochester, 724 Computer Studies Building, Box 270231, Rochester, NY 14627, United States of America

E-mail: kevin.parker@rochester.edu

Keywords: brain, optical elastography, sleep/wake cycle, microchannel flow model, reverberant shear wave fields

Abstract

As elastography of the brain finds increasing clinical applications, fundamental questions remain about baseline viscoelastic properties of the brain *in vivo*. Furthermore, the underlying mechanisms of how and why elastographic measures can change over time are still not well understood. To study these issues, reverberant shear wave elastography using an optical coherence tomography scanner is implemented on a mouse model, both under awake conditions and in a sleep state where there are known changes in the glymphatic fluid flow system in the brain. We find that shear wave speed, a measure of stiffness, changes by approximately 12% between the two states, sleep versus awake, in the entire cortical brain imaging volume. Our microchannel flow model of biphasic (fluid plus solid) tissue provides a plausible rheological model based on the fractal branching vascular and perivascular system, plus a second parallel system representing the finer scale glymphatic fluid microchannels. By adjusting the glymphatic system fluid volume proportional to the known sleep/wake changes, we are able to approximately predict the measured shear wave speeds and their change with the state of the glymphatic system. The advantages of this model are that its main parameters are derived from anatomical measures and are linked to other major derivations of branching fluid structures including Murray's Law. The implications for clinical studies are that elastography of the brain is strongly influenced by the regulation or dysregulation of the vascular, perivascular, and glymphatic systems.

1. Introduction

Elastography of the brain is a relatively new and exciting technology that promises to provide sensitive biomarkers related to the viscoelastic properties of the brain (Hiscox *et al* 2016, 2018, Bigot *et al* 2018, Gerischer *et al* 2018, Munder *et al* 2018, Guo *et al* 2019, Murphy *et al* 2019, Arani *et al* 2021). At this early stage of study, we know that there are changes in brain viscoelastic properties with age, injury, and disease, but the basic understanding of *why* these changes occur and *how* they are linked to the tightly regulated brain vascular, perivascular, and glymphatic fluid systems, requires careful investigations.

We are now able to integrate recent major advances in our understanding of the intricate systems of fluid flow in the brain, their key role in health and the progression of disease, and their strong influence on biomechanics and elastography biomarkers. The first key fact is that the neurovascular unit (NVU) and glymphatic system are strongly regulated in the healthy brain. Progressive dysregulation can occur with aging and Alzheimer's disease. Secondly, a recent discovery is that there are major changes in the flow of extracellular fluids throughout the glymphatic system, within the normal sleep/wake cycle (figure 1) and in aging and disease. For example, flow increases during sleep or anesthetized states, which increases the rate and clearance of beta-amyloid protein, a neurotoxin associated with Alzheimer's disease (Xie *et al* 2013, Rasmussen *et al* 2022). Impaired flow has dire consequences for the brain over the long term. Our third conceptual point is that in complex biomaterials like the brain, changes in the size or distribution of pores and fluid channels will create a major change in stress–strain responses, which are readily assessed by elastography techniques. In other words,

© 2022 Institute of Physics and Engineering in Medicine

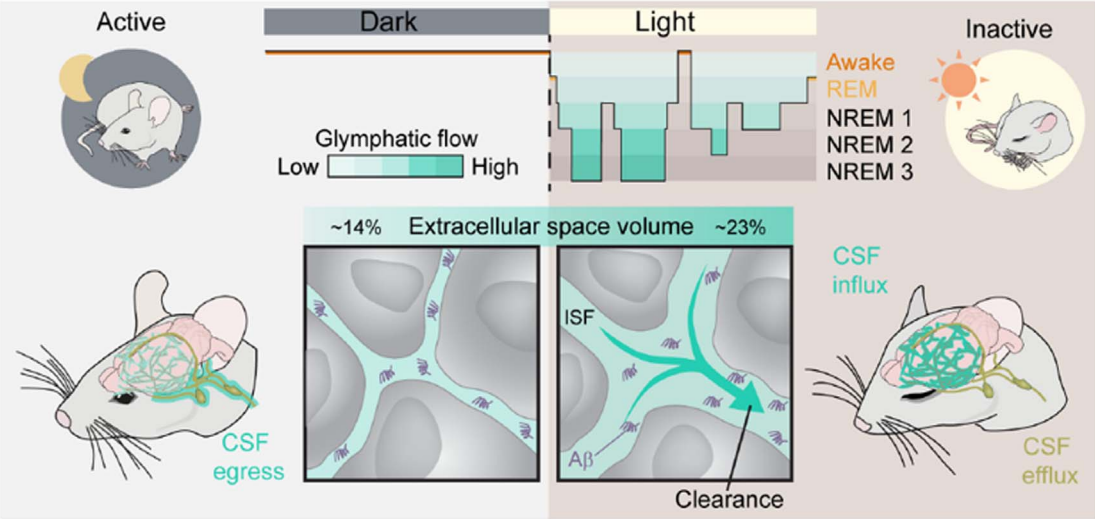

Figure 1. Glymphatic activity and cerebrospinal fluid (CSF) egress in the nocturnal mouse during active phase (upper left, under darker surroundings), and during sleep (upper right). The glymphatic system is active during deep sleep, when brain clearance more than doubles compared with wakefulness. This is due to an increase in extracellular volume fraction, which in rats is ~14% during wakefulness but increases to 23% in a process dependent on the loss of noradrenergic signaling from the locus coeruleus (Xie *et al* 2013). This could occur by a mechanism whereby perivascular space access is shut off during periods of high noradrenergic tonus, but then opens up for fluid influx during the low noradrenergic tonus of sleep. The rate of CSF egress from the subarachnoid space shows an inverse relationship with glymphatic activity, thus increasing during wakefulness and decreasing during sleep (Ma *et al* 2019). Top row: the relationship between sleep and glymphatic activity. Bottom row: the critical importance of the extracellular volume fraction on glymphatic flow in the active state (left) and during inactivity [non-REM (NREM) sleep, right]. Reproduced with permission from Rasmussen *et al* 2022. Copyright © 2022 the American Physiological Society.

we hypothesize that as channel or pore size *increase*, hydraulic resistance *decreases*, (fluid can flow more freely) and, correspondingly, elastography measures of stiffness will decrease. This causal link has been supported in theory (Parker 2014, 2017a) and in experiments in a number of tissues (Parker 2015, Parker *et al* 2016, Poul *et al* 2020), and in this study of animal models during sleep/wake cycles using optical coherence tomography (OCT) elastography. These novel results are presented herein and the theoretical basis for interpreting the changes in tissue stiffness, as measured by shear wave elastography, is the major subject of this paper. Among the many rheological frameworks for modeling the brain (Audette *et al* 2007, Klatt *et al* 2007, Budday *et al* 2017, Testu *et al* 2017, Comellas *et al* 2020), our approach has a number of advantages in that its parameters are tied to anatomical measures, it is biphasic and can account for changes in fluid channels, and it is based on power laws. The power law framework, related to fractal branching vascular and other multiscale channels, has a well-established set of interconnected parameters such as flow resistance which are also relevant to the overall biomechanical and functional assessment of the brain. This paper is organized to provide an overview of the theoretical approach employing the microchannel flow model, then describing experimental results of sleep versus wake elastography in an *in vivo* mouse OCT protocol. Model predictions are made using reasonable parameters that match the observed changes in shear wave speeds (SWSs) in the cortex obtained in this study. Finally, the appendices further detail the derivation and anatomical link of the key parameters, and their change with dilation or constriction.

2. Theory

2.1. Structure and function

The larger goal is to identify the key determinants of viscoelasticity in the brain, along with major cofactors, trends, species, and regional variations. In this study our experimental results are compared with the microchannel flow model, which captures the biphasic (fluid, solid) nature of the brain (Parker 2014, 2017a). Briefly, the microchannel flow model accounts for the movement of fluids within channels in soft tissues, forming a biphasic rheological model that can predict how shear waves (and elastography measures) will change as fluid channels dilate or constrict. The model also has some resemblance to a generalized Maxwell model and the Kelvin–Voigt fractional derivative model, however our model accounts explicitly for the distribution of fluid channels within the parenchymal matrix. Figure 2 shows the major components captured in the microchannel flow model, including the vascular, perivascular, and the interstitial microchannels. Each of these are highly regulated in the healthy brain with rigid constraints on fluid volume within the skull, and these factors are

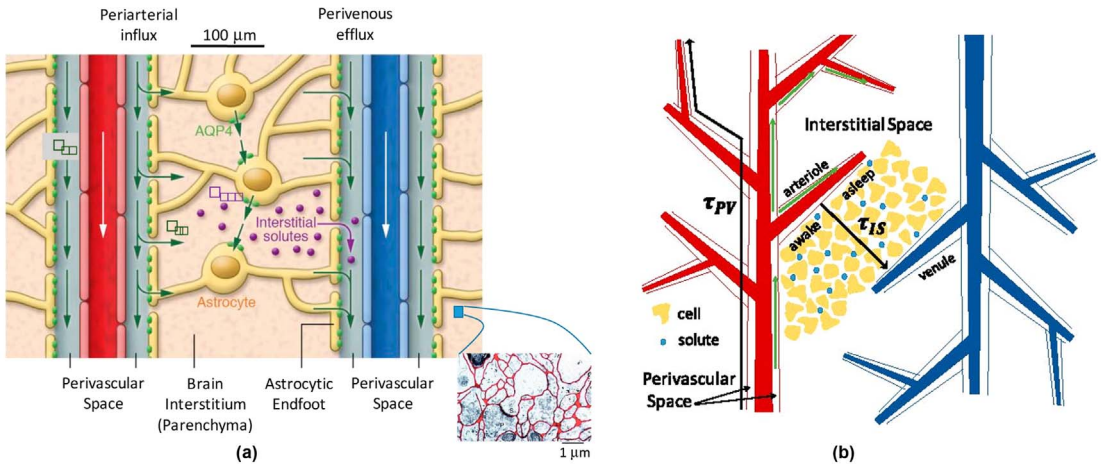

Figure 2. (a) Illustration of details within brain tissue. Arterioles and venules penetrate the tissue, each surrounded by perivascular space (PVS). The blood-vessel wall forms the inner barrier of the PVS, note the tight junctions between cells. Astrocytic endfeet form the outer barrier of the PVS, with looser gaps between cells allowing transport into the interstitium. The interstitium is crowded with cells where both fluid and solutes move along a tortuous path in a restricted extracellular liquid volume that comprises approximately 20% of the total volume (see insert). Green arrows indicate fluid transport, by advection and diffusion. In the glymphatic hypothesis, fluid moves along the periarterial space into the interstitium and out along the perivenous space. Purple indicates interstitial solutes; solutes exit the interstitial space through gaps in the astrocytic endfeet to the perivenous space, where they are cleared to primary perivenous pathways or the CSF. (b) A cerebral penetrating artery and vein with perivascular space. Fluid (green arrows) moves into the brain along periarterial space, branching into arteriole PVS. Characteristic length for periarterial transport is the entire path from penetrating artery to terminating arteriole (drawing not to scale). From periarterial space, fluid enters the interstitium and moves to perivenous space. Reproduced from Ray and Heys 2019. CC BY 4.0.

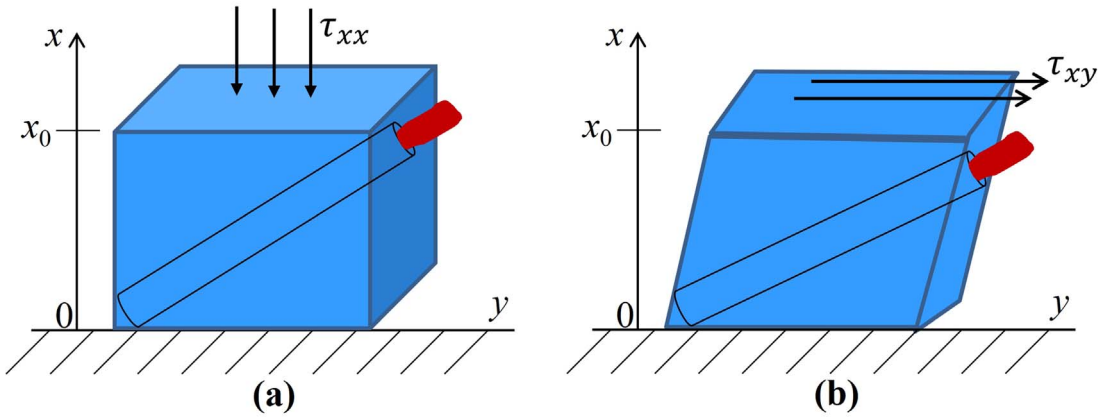

Figure 3. Elastic element with a single vessel undergoing (a) uniaxial stress or (b) shear stress. The fluid-filled microchannel will experience flow to the free surface (right) thus contributing to the relaxation response. Reproduced from Parker 2017b. © 2017 Institute of Physics and Engineering in Medicine. All rights reserved.

necessary ingredients in a predictive model (Parker 2017a). The microchannel flow model is, to our knowledge, the most succinct rheological model capable of accounting for all three fluid networks shown in figure 2 (vascular, perivascular, interstitial) with careful accounting for the relative proportions of these within the fixed volume of the skull, and the fractal nature of the vasculature (Parker 2017a). Refining the key parameters to fit the measured shear moduli will be helpful to the basic science of elastography of the brain along with its implications for clinical assessments.

2.2. Review of microchannel flow theory of stress–strain in vascularized tissues

The microchannel flow model (Parker 2014) can be formulated with an elastic block of tissue, containing one vessel of radius r and supported at the base and subjected to uniaxial loading. An example of uniaxial strain or alternatively shear is shown in figures 3(a) and (b), respectively.

When the fluid within a microvessel of length L and radius r is exposed to a pressure gradient due to applied stress σ_x, then under Poiseuille's Law, a volumetric flow rate Q will result (Sutera 1993):

$$Q = \frac{C\sigma_x r^4}{\eta}, \tag{1}$$

where C is a constant, and η is the viscosity of the fluid. Combining both the elastic and fluid outflow strains as additive leads to the well-known Maxwell model of a series spring and dashpot, therefore the stress relaxation (SR) curve is a simple exponential decay. If we apply a step strain and measure the stress relaxation, then

$$\sigma_{SR}(t) = \varepsilon_0 E \mathrm{e}^{-t/\tau} \text{ for } t \geqslant 0, \tag{2}$$

where E is the Young's modulus of the elastic block of tissue and the time constant τ is:

$$\tau = \frac{\eta C}{E r^4}. \tag{3}$$

The inverse relationship of τ to radius to the fourth power indicates that stress relaxation is sensitive to changes in vessel radius. In appendix A this derivation is modified for the case of many small vessels with a number density $N(r)$ that is a power law function of radius, as illustrated in figure 4(b).

Accordingly, in a macroscopic block of tissue we assume there are n multiple microchannels of unequal radius r_n and a range of flow rates Q_n. Assuming each contributes to the overall stress relaxation with an individual time constant τ_n, then the simplest model for this looks like a parallel set of Maxwell elements shown figure 4(c). This also resembles the generalized Maxwell–Weichert model (Ferry 1970, Fung 1981). In the limit, we model a continuous distribution of time constants τ, where $A(\tau)$ is the relaxation spectrum (Fung 1981). Given a material's $A(\tau)$, we then have:

$$\sigma_{SR}(t) = \int_0^\infty A(\tau)\mathrm{e}^{-t/\tau} d\tau. \tag{4}$$

In some tissues we find a power law distribution:

$$A(\tau) = A_0 \tau^{-b}; \quad 1 < b < 2, \tag{5}$$

which is naturally occurring in many natural structures including normal and pathological circulatory systems (West *et al* 1997, Risser *et al* 2007), and which is justified in appendix A based on anatomical measures. Substituting equation (5) into equation (4) and solving yields the stress relaxation behavior:

$$\sigma_{SR}(t) = \mathrm{A}_0 \cdot t^{1-b}\Gamma[b-1] \text{ for } 1 < b < 2, \ t > 0, \tag{6}$$

where $\Gamma[\,]$ is the Gamma function. The stress relaxation response produces a $1/t^{b-1}$ decay for $t > 0$ as illustrated in figure 4(f). For values of $1 < b < 2$, this tends to have a sharp initial drop and then a slow asymptomatic decay and produces a straight line on log–log plots. In this case the frequency dependence of the complex modulus is given by an increasing power law:

$$|E(\omega)| = \frac{A_0}{\sqrt{2\pi}}\Gamma[a]\Gamma[1-a]\ |\omega|^a, \tag{7}$$

where $a = b-1$.

It may be more realistic to place limits on the range of τ for a material, where the longest and shortest time constraints correspond directly to the smallest to largest vessels and microchannels, as illustrated in figures 4(a)–(d). In this case, the integration of equation (4) has limits $\tau_{\min}$ and $\tau_{\max}$ and

$$\sigma_{\mathrm{SR}}(t) = \int_{\tau_{\min}}^{\tau_{\max}} A(\tau)\mathrm{e}^{-t/\tau} d\tau, \tag{8}$$

and assuming the power law form of equation (5), then

$$\sigma_{\mathrm{SR}}(t) = A_0 \left(\frac{\Gamma\left[a, \frac{t}{\tau_{\max}}\right] - \Gamma\left[a, \frac{t}{\tau_{\min}}\right]}{t^a} \right) \text{for } a > 0, \ t \geqslant 0, \text{ and } 0 < \tau_{\min} < \tau_{\max}, \tag{9}$$

where $\Gamma[a, \ (t/\tau)]$ is the incomplete Gamma function (upper-tailed). This produces a four-parameter model since $\tau_{\max}$ and $\tau_{\min}$ are vessel-specific parameters (determined from anatomy studies) in addition to a and A_0. The complex modulus $|E(\omega)|$ for the material of equation (9) is derived from Laplace transform relationships and solved using Mathematica (version 13.1.0 for Linux x86, Wolfram, Champaign, IL, USA). With ω representing radial frequency, and I the imaginary unit index, we find the complex solution to be:

$$E(\omega) = A_0(-I\omega)(\beta[(-I\omega\tau_{\min}), (1-a), 0] - \beta[(-I\omega\tau_{\max}), (1-a), 0]), \tag{10}$$

where $\beta[]$ is the incomplete beta function (Abramowitz and Stegun 1964). Basically, this function approaches a simple power law of equation (7), but only in between lower and higher frequencies defined by $1/\tau_{\max}$ and $1/\tau_{\min}$, and assuming these are widely separated in a multiscale structure.

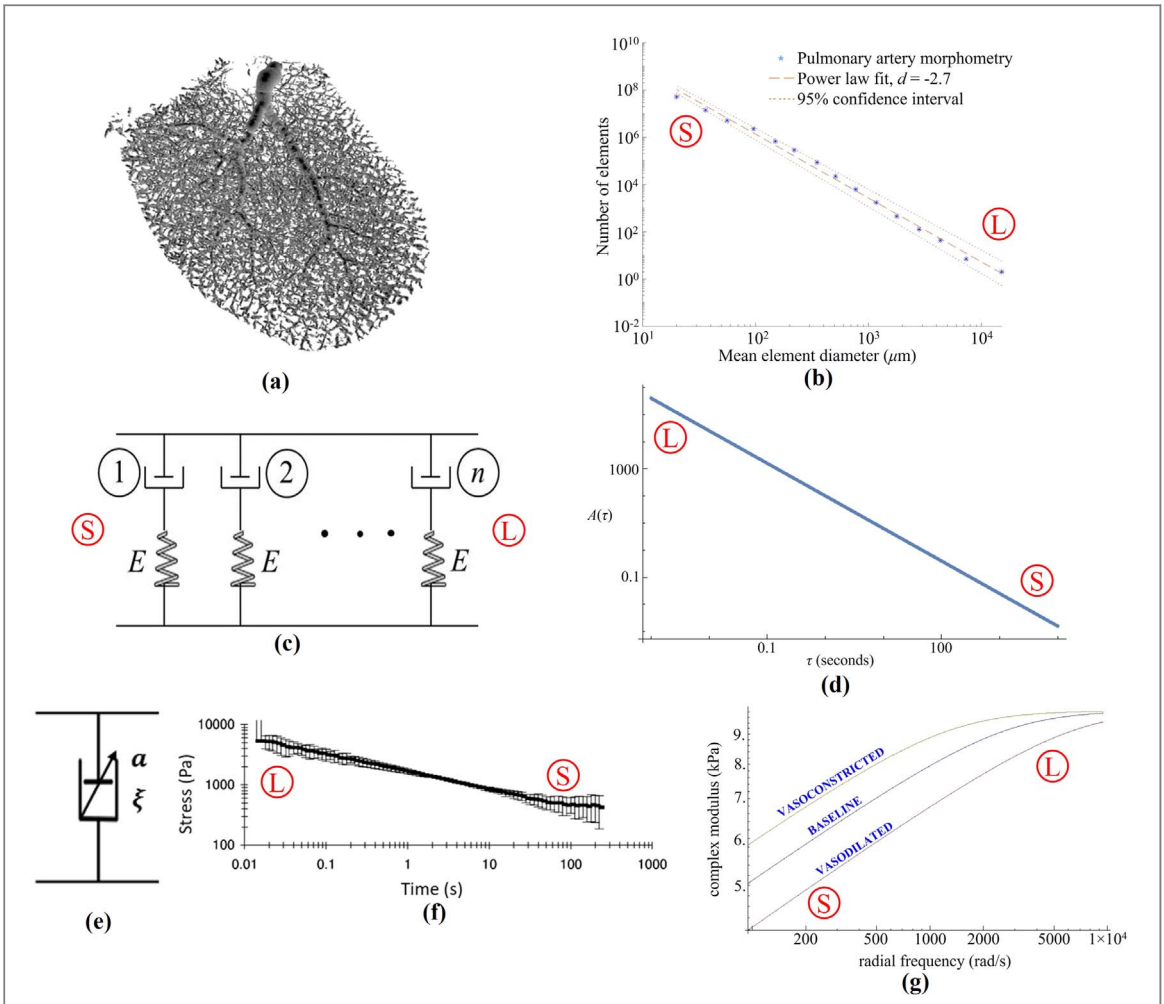

Figure 4. The conceptual framework of the microchannel flow model, with inter-relationships between key elements and their behaviors. (a) Fractal branching vasculature from a vascular cast, imaged with micro-CT (Parker 2022). This fractal branching structure ranges from a larger set of vessels to a smallest set. In the following figures, circle *L* and *S* refer to regions that are particularly influenced by the largest and smallest fluid channels within the ensemble. (b) Power law relationship between element diameter and quantity in pulmonary arteries, extracted from data in Huang *et al* (1996) and veins. Power law fit $d = -2.7 \pm 0.1$. (c) The microchannel flow model of perfused soft tissue begins with parallel elements (Parker 2014). Each dashpot corresponds to a fluid-filled vessel or channel, with the smallest microchannel yielding the longest time constant, via Poiseuille's Law. In the continuous limit, the aggregate sum over the fractal size distribution yields the microchannel flow model. (d) The relaxation spectrum is formed by the power law distribution of vessels and the time constants extend from less than one second (due to larger vessels) to very long (due to small capillaries and extracellular fluid channels). (e) In simplest form, the combination of these elements reduces to a simple rheological model: the spring-pot model (a simplified KVFD model) which can be described succinctly through a fractional derivative model. The fractional order is explicitly linked to the power law distribution of the fluid channels shown in (b). (f) Stress relaxation results from two liver samples. Vertical axis: measured stress. Horizontal axis: time in seconds after stress compression, on a log–log scale. The behavior is consistent with a power law relaxation. Reprinted from Liu and Bilston (2000). (g) Complex modulus versus frequency for a nominally soft vascularized and unconfined tissue over a range of frequencies from $2\pi{\cdot}15$ to $2\pi{\cdot}1500$ Hz, plotted on a log–log scale. The model indicates an increase (or decrease) in the complex modulus and SWS when the branching fluid channels are constricted or dilated, respectively.

In summary, if a tissue has a power law distribution of fluid vessels and channels, and a relaxation spectrum $A(\tau) = A_0\tau^{-b}$, then the stress relaxation response behavior is $\sigma_{SR} \cong A_0 t^{1-b} = A_0/t^a$. The tissue stress–strain transfer function, or complex modulus, in the frequency domain resembles $|E(\omega)| \cong A_0\omega^a$, and the shear wave phase velocity $c_{ph}(\omega) \propto \omega^{a/2}$. We have found that $0 < a < (1/4)$ for many normal soft vascularized tissues (Zhang *et al* 2007, Parker 2014, Ormachea *et al* 2016).

2.3. Specific components of the brain microchannel flow model

As shown in figure 2, a full model of the brain fluid channels would include at least the following five components: the arterial, periarterial, venous, perivenous, and interstitial (glymphatic) channels within the brain parenchyma. These are modeled herein as two interconnected but separate fractal systems: the larger comprised of the parallel vascular and perivascular branching structures over a scale of approximately 1 mm to 4 microns in radius, and then the smaller fractal structure within the tortuous interstitial space, covering a scale from about 1 micron (gaps in the astrocytic endfeet locations) to approximately3 angstroms (AQP4 pore size), as

indicated in figure 2. Both systems are tightly regulated in the brain in normal individuals; the NVU regional control is assessed in functional magnetic resonance imaging scans, angiography, and other tests, while the glymphatic regulation under sleep/wake cycles is a more recent discovery and the main focus of this model. The vasculature and perivasculature are naturally described as fractal systems (Risser *et al* 2007, Parker 2017a), however the interstitial/glymphatic networks require additional justification. First, following Murray's law of fluid transport, a great many biological systems employ a scale invariant, power law, or fractal organization as an optimum configuration (Sherman 1981, Hughes 2015). Secondly, in optical studies of other organs, power law behaviors are seen down to a scale on the order of 10 nanometers (Schmitt and Kumar 1996). Thirdly, the multiscale organization of the interstitial space is suggestive of a power law model (Nicholson 2022). We therefore assume a two compartment blend of the microchannel flow model of equation (9): a larger scale version representing the vascular and perivascular branching structures and a smaller scale version representing the interstitial spaces:

$$\sigma_{SR}(t) = A_1\left(\frac{\Gamma\left[a, \frac{t}{\tau_{max}}\right] - \Gamma\left[a, \frac{t}{\tau_{min}}\right]}{t^a}\right) + A_2\left(\frac{\Gamma\left[a_2, \frac{t}{\tau_{2_{max}}}\right] - \Gamma\left[a_2, \frac{t}{\tau_{2_{min}}}\right]}{t^{a_2}}\right), \tag{11}$$

where A_1 represents the vascular and perivascular fractal branching structures and A_2 the smaller scale interstitial/glymphatic structures. The time constants will be set by the largest and smallest channels expected within each of these. The parameters are conditioned by anatomical measures and are discussed in more detail in the appendix A, although the parameters for mouse and human brain regions require refinement. The complex modulus as a function of frequency will then be given by the sum of two corresponding groups of beta functions given by equation (10), and the SWS as a function of frequency (the phase velocity and dispersion) can be calculated from this quantity. As a practical matter, the pores and channels in the glymphatic system are very small, extending to well below 1 micron. Correspondingly, the time constants for the glymphatic system are proportionally long, and so the influence of these long time constants at typical elastography frequencies (roughly 40–100 Hz in adult human magnetic resonance elastography) approaches an asymptotic limit. Thus, in elastography, the glymphatic compartment term approximates an additive constant in equation (10) of $(1/\tau_{min}^{a_2})(A_2/a_2)$ for $a_2 > 0$ and for frequencies $\gg 1/\tau_{min}$. Consequently, our simplified model for the complex modulus in the frequency domain for the brain, accounting for both the neurovascular and the glymphatic systems, may be expressed as:

$$E(\omega) = A_1(-I\omega)(\beta[(-I\omega\tau_{min}), (1-a), 0] - \beta[(-I\omega\tau_{max}), (1-a), 0]) + (A_2/\tau_{min}^{a_2})(1/a_2) \tag{12}$$

for $a > 0$ and $\omega \gg 1/\tau_{min}$. Dilation or constriction of either of the two compartments can be treated simply with scale factors shifting both the magnitude and the time constants, as described in appendix B.

3. Methods

3.1. Animal preparation

Five wild-type mice (C57BL/6, mean 9.21 $\pm$ 0.13 months of age, 3 female/2 male) were scanned with OCT elastography in both awake and anesthetized (mimicking sleep) states. Mice were habituated to the scanning apparatus and prior to scanning, cranial window surgeries were performed in which a 5 mm diameter circular region of center skull was replaced with a glass window. The dura mater was left intact, and 1.1% agarose gel was used to adhere the glass window to the brain. A rectangular head plate and mounting station was used to secure the mouse head and body during both awake and anesthetized states. After the cranial window surgery, the mouse was allotted at least 30 min to wake before scanning. Upon completion of the awake scan, the mouse was injected with ketamine–xylazine and allotted at least 15 min before scanning the sleep scan. Mice experiments were performed under protocols approved by the University of Rochester Committee on Animal Resources. Figure 5 shows the experimental setup with respect to the mouse.

3.2. Optical coherence tomography

A custom phase-sensitive OCT and mechanical piezo-electric system was used to scan the mice and perform reverberant shear wave (RSW) elastography. The OCT system source is a swept-source laser (HSL-2100-HW, Santec, Aichi, Japan) with a center wavelength of 1310 nm and a bandwidth of 140 nm. The lateral resolution is approximately 20 μm and the axial resolution is approximately 6 μm in air. The field of view for these experiments was 5 $\times$ 5 mm. The OCT system is controlled using LabVIEW (version 14, National Instruments, Austin, Texas, USA).

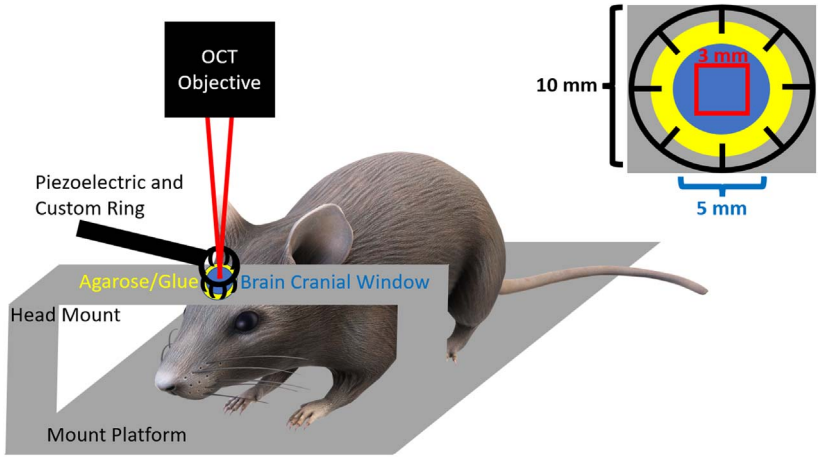

Figure 5. Experimental setup with mouse scans (not to scale). The top right corner depicts the dimensions of the cranial window (blue) with respect to the custom ring (black) and region of interest analyzed (red).

3.3. Reverberant shear wave elastography

RSW elastography is implemented with a mechanical excitation system that operates in conjunction with the OCT scanning system. The main piezo-electric controlled component is a custom 10 mm diameter 3D-printed ring with 8 concentric points of contact that generates multiple shear waves inside the brain region of interest (ROI). The rings' tips are in physical contact with the agarose gel that supports the cranial window but are not in physical contact with the brain. The function generator used for the piezo-electric actuator was operated at a frequency of 2 kHz. The MB mode acquisition approach acquires 4D data (3D space and time) in a synchronized fashion, with 100 A-lines by 100 frames by 100 M-modes with an axial depth of 2000 points. For each individual point in time in which a fully developed 3D RSW pattern is present, 2D local spatial autocorrelations (in x–y plane) are performed in window sizes of 1×1 mm with window intervals of 0.5×0.5 mm along each point in depth. From this, a 3D map of local wavenumbers is obtained, which can then be converted to local SWS. Subsequently, the estimated 3D elastograms from each timepoint in the acquired data are averaged together to generate the final elastogram. More details on the OCT and mechanical excitation system can be found in previous studies using OCT elastography to evaluate corneas (Zvietcovich *et al* 2019, Ge *et al* 2022).

3.4. Statistical analysis

From the 3D elastograms, homogeneous ROIs are selected to obtain mean SWS results. In the awake scans, mouse ROIs included are the brain parenchyma (BP) and the perivascular (PV) regions, where the boundary is distinct. In the sleep scans, the boundary between BP and PV can be less distinct, and pre-calculations indicated there were no statistical differences between the two regions (using a t-test), and so a single sleep SWS is reported for the entire homogeneous ROI. With these multiple groups of mice scan types, a one-way ANOVA test is performed with a subsequent Bonferroni-corrected multiple comparisons test. Statistical significances are assigned as follows: no significance (NS) for $p > 0.05$, * for $p < 0.05$, ** for $p < 0.01$, *** for $p < 0.001$, and **** for $p < 0.0001$.

4. Results

Application of 2 kHz shear waves to the cranium with multiple contact points creates a randomized pattern of shear waves that we classify as a RSW field, with a characteristic 'boiling' pattern shown in figures 6(b) and (e). Estimators then assess the local value of SWS (Parker *et al* 2017, Ormachea and Parker 2021) which are displayed in colors within the 3D scanned volume as shown in figure 6. In the cranial window, major vessels can be resolved and the proximal region surrounding them may appear softer than the more distal parenchyma, see figure 6(c). Repeatably, the brain in the sleep state (mean of 2.17 ± 0.05 m s^{-1}) is softer than in the awake state (mean of 2.46 ± 0.04 m s^{-1} in brain parenchyma), as indicated in figures 6(f) and 7. SWS in the awake state for the cortical region drops nearly 12% in the sleep state. The SWS of the perivascular region in the awake state (mean 2.16 ± 0.05 m s^{-1} in perivascular region) was statistically similar to the SWS of the sleep state (mean of 2.17 ± 0.05 m s^{-1}).

Using equation (12), a corresponding model of the complex modulus was generated and is plotted in figure 8 on a log–log scale over a range of shear wave frequencies from 1 to 3 kHz. The dashed lines indicate the level of

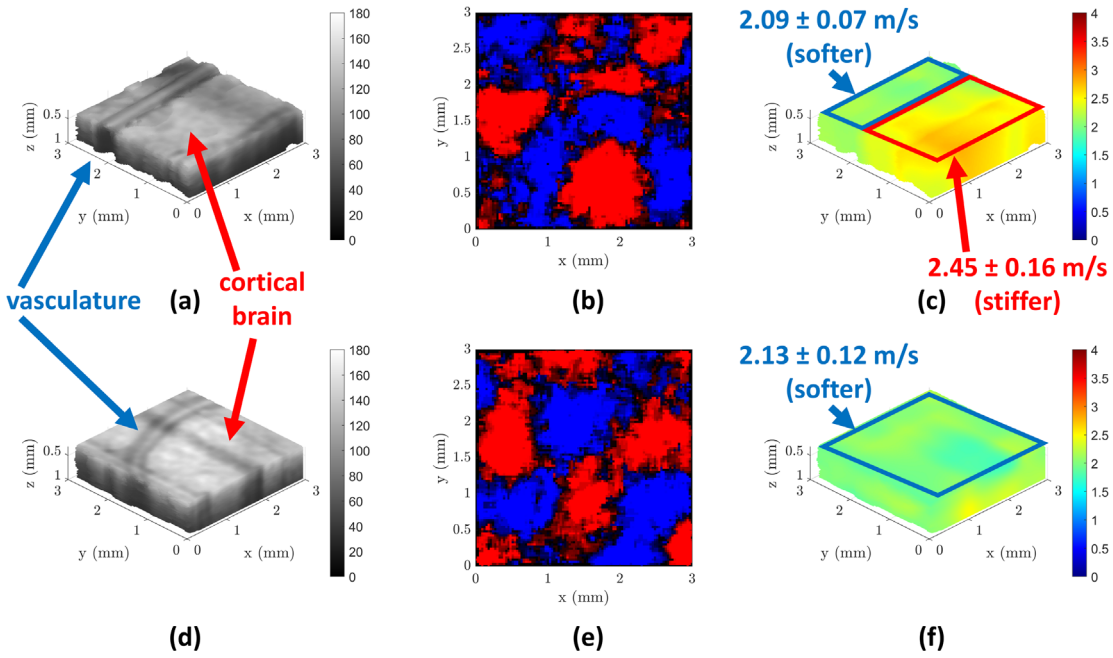

Figure 6. OCE of mouse brain *in vivo*. (a) 3D B-mode scan in awake state. (b) Sample transverse plane (at $z = 0.57$ mm) of measured 2 kHz shear wave pattern. (c) Reconstructed 3D elastogram showing regional stiffness variation between perivascular regions ($y > 2$ mm) and surrounding brain parenchyma ($y < 2$ mm). (d) 3D B-mode scan in anesthetized state (with ketamine–xylazine). (e) Sample transverse frame (at $z = 0.57$ mm) of measured 2 kHz shear wave pattern. (f) Reconstructed 3D elastogram showing stiffness homogenization after anesthesia with KX to simulate sleep state. We hypothesize that this softening is directly related to the change in glymphatic system morphology and CSF egress, as depicted in figures 1 and 2. Elastogram shear wave speed values are reported in meters/seconds as mean ± standard deviation in 3D ROI. Units of color bars in (a) and (d) are in arbitrary grayscale values; units of color bars in (c) and (f) are in m s^{-1}.

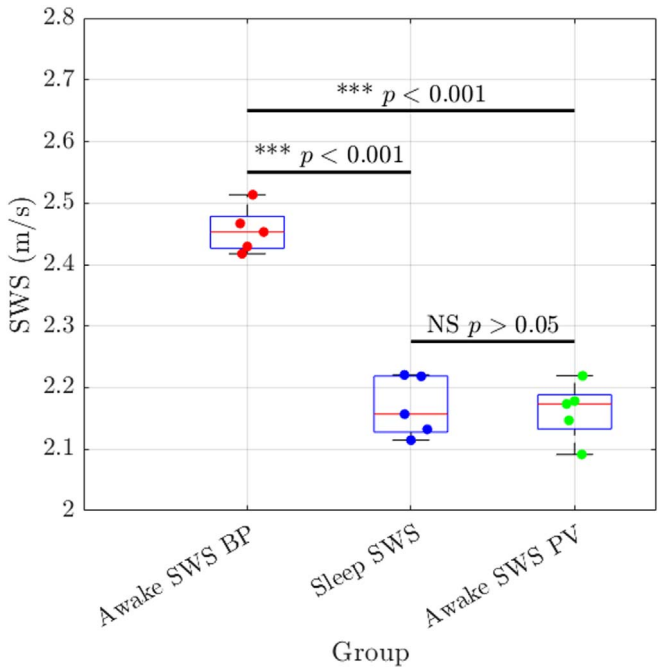

Figure 7. Measured shear wave speeds (SWS) in the cortical brain at 2 kHz for groups of wild-type mice in sleep and awake conditions. The 3D regions are denoted in figure 6 and BP = the brain parenchyma or cortex, PV = perivascular region surrounding a resolved vessel. We find a statistically significant drop in shear wave speed of approximately 12% from awake to sleep, hypothesized to be influenced by changes in the glymphatic system.

complex modulus expected given the measurements shown in figures 6 and 7 for both awake and sleep states at 2 kHz. The model fits for both the awake and sleep states demonstrate a monotonic increase throughout the frequency range, indicating dispersion associated with viscoelastic losses, and tends to flatten near the upper

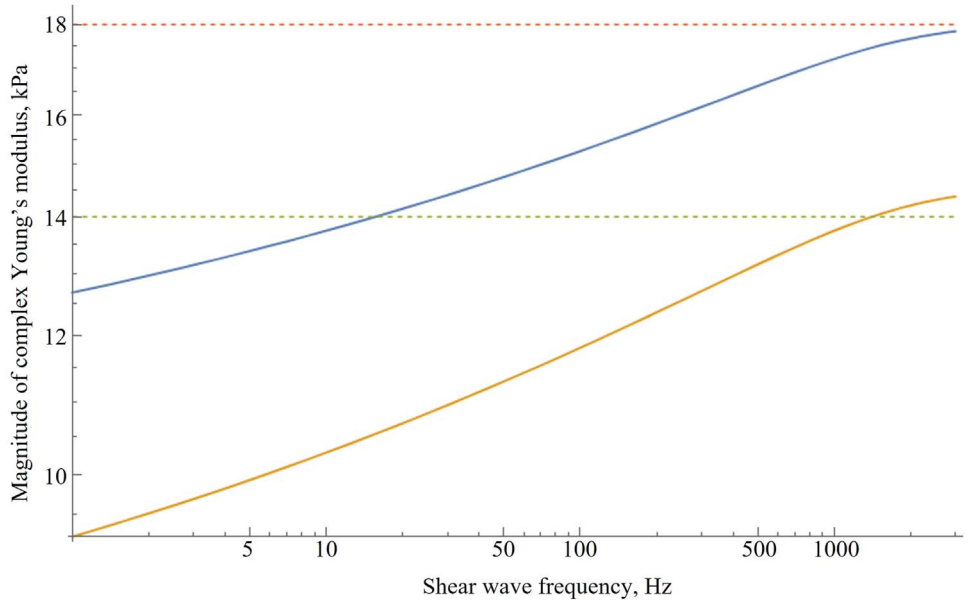

Figure 8. Theoretical values of complex modulus (vertical axis) magnitude versus shear wave frequency (horizontal axis). Dotted lines represent the approximate bounds of measured values at 2 kHz, based on the results of figure 7. Solid lines represent the model results with awake (top curve blue) and sleep (lower curve, yellow). A_1 for the vascular system is taken as 0.38 Pa, power law exponent a is 0.15. For the glymphatic compartment, A_2 is higher than A_1 (2 $\times$ higher density of fluid channels) and a is 0.05, corresponding to a higher branching exponent of b than the vascular system, approaching $b = 2.95$ and close to Murray's Law where b would approach 3. The dilation (lower curve) is a factor of 1.28 increase in radius throughout the glymphatic fluid channels, corresponding to an overall increase in glymphatic fluid percent volume (23%/14% attributed to increases in radius squared across the entire range of microchannels in the glymphatic system) depicted in figure 1 during sleep cycles as compared with awake cycles.

Table 1. Baseline parameters used in the microchannel flow model of the brain incorporating the terms in equation (12) and their constituent elements.

Parameter	Value	Units	Comments
E_0	1	kPa	unitary, also very soft tissue
b, (a)	1.05–1.25, (0.05–0.25)	dimensionless power	power law from anatomy
A_1	0.38	Pa·s^a	related to $N(r)$ of vasculature and perivasculature
A_2	0.76	Pa·s^a	related to $N(r)$ of glymphatic system
$\tau_{1_{\min}}$	0.0005	s	related to largest radius or free fluid interface
$\tau_{1_{\max}}$	23	s	set by capillary size
$\tau_{2_{\min}}$	190	s	set by glymphatic space openings
$\tau_{2_{\max}}$	10^8	s	set by AQP4 pore radius, and assumed to approach infinity in equations (11), (12)
χ	1.28	ratio	dilation of glymphatic system
η	1.5×10^{-3}	Pa·s	plasma and extracellular fluid viscosity

range of frequencies (3 kHz) as this extends beyond the fastest time constants in the model. In reality, other loss mechanisms not included in the model, including viscous terms in the parenchymal constituents and scattering of the shear waves, could become significant at higher frequencies and thereby continue the dispersion. Accounting for additional loss mechanisms remains for future studies. Table 1 provides the estimated values employed in the model of equation (12) and figure 8, and we note that no attempt has been made to derive a maximum likelihood estimate of the model parameters; that remains for future research.

5. Discussion

We have measured subtle sleep/wake changes in the stiffness of the cortical region of the mouse brain using OCT with RSW field elastography. The simplest rheological model of this is the biphasic model of fluid in a cellular parenchyma, the microchannel flow model which is compartmentalized in equation (11) into the NUV and the glymphatic or extracellular system. It may appear at first glance that this equation requires the precise assessment of eight unknown parameters, [A, a, $\tau_{\max}$ $\tau_{\min}$], for each of the neurovascular and glymphatic

compartments. However, this is reduced by recognizing the asymptotic form of the glymphatic system's contribution for typical elastography frequencies in equation (12). Furthermore, as detailed in appendix A, the parameters a, τ_{max}, and τ_{min} are bounded by Murray's law and continuity arguments and can be determined by anatomical imaging studies that quantify the multiscale distribution of vessels and fluid channels within the brain. These require painstaking efforts with high resolution 3D imaging systems, and more comprehensive studies and results are needed to refine these parameters in normal and disease conditions.

It can be noted that the microchannel flow model for the brain components has the advantages of both a simplicity and a framework that relates immediately to the extensive literature on the properties of fractal branching structures. In particular, there are inter-related power law exponents for a number of physiological variables including flow, flow resistance, pressure, fluid volume, and others that can be calculated using many of the anatomical parameters discussed in our model (Kassab 2006, Kamiya and Takahashi 2007, Mut *et al* 2014, Razavi *et al* 2018). The model thereby provides a close interconnection between elastography and the hemodynamics and glymphatic flow in the brain. For completion, it should be noted that there are other classical models that could be applied to the rheology of the glymphatic system. These include the poroelastic models based on Biot's approach (Biot 1941, 1962, Konofagou *et al* 2001). Furthermore, a range of composite material models has been formulated for determining the effective modulus of a material comprised of two or several components, including the strain energy analysis of Christensen (1969). Composite material properties are described and compared in detail in Lakes (1999), including Voigt and Reuss bounds on the properties of the composite models. In our case, using the Christensen model for nearly incompressible tissue (see equations (1), (2) in Ormachea and Parker (2022)) with the shear modulus of fluid areas set to zero, we can estimate a sleep/wake change in the composite glymphatic tissue where volume percent V of fluid changes from 23% to 14% as shown in figure 1. The result is a predicted increase in shear modulus of 24%, higher than the experimental change of 12% shown in figure 7. Let us note that the glymphatic system is only one component of the brain, so further research will be required to elucidate the competitive advantages of different approaches to an accurate rheological model.

Some of the limitations of this study include the limited number of mice studied, and the need for wider range of frequencies used for shear wave excitation. Another important limitation of the model itself, along with the need for more precision in key parameters and exponents, is that the model may be oversimplified in a number of respects. For example, a single value for viscosity has been used, however the apparent viscosity of plasma is thought to be a function of vessel diameter in the micron range (Kamiya and Takahashi 2007). Another example is the length to radius relationship of vessels, which is likely to vary between smaller and larger fluid channels, and also may vary by region within the cortical structures (Cassot *et al* 2006). Also, the model does not explicitly consider anisotropic alignment of structures and nonlinear behavior. In these cases, further refinements can be made but at the expense of additional complexity. For now, the model presented incorporates single values of parameters over these possible variations, utilizing estimates from tables 1 and A1.

Another limitation of this study is the use of ketamine–xylazine anesthesia to induce sleep. This particular protocol is known to produce changes in the glymphatic system commensurate with sleep (Rasmussen *et al* 2022). However, as shown by Turner *et al* (2020), natural REM and non-REM sleep states in mice demonstrate major changes in cerebral blood volume, and increased arterial diameters along with increased neuronal activation. In our case, the contact with piezo-electric shear wave actuators makes natural sleep difficult. These conditions remain for further study in terms of their effects on elastography measures and the microchannel flow model.

We also note that rapid 10% changes in the shear modulus in the mouse thalamus region were reported by Patz *et al* (2019), during activation by sensory stimulation. The underlying mechanism of these changes were thought to be related to several effects including the blood oxygenation changes during stimulation and calcium ion transport. Some calculations pertinent to change in the underlying tissue properties, captured in the parenchymal E_0, have been considered previously in Parker (2017a), along with changes in the vascular and perivascular structures in a strictly confined space. All these effects are potentially able to alter the SWS in elastography measurements. It remains to be seen if a combination of these is present and influential in human brain elastography, however the microchannel flow model can model these individually or in combination.

6. Conclusion

The sleep/wake cycle of the brain is found to influence the elastography measure of SWS in the mouse brain. Specifically, in the cortical brain parenchyma and with RSWs at 2 kHz, we find a softening of the brain by an approximately 12% drop in SWS during anesthesia-induced sleep as compared with awake status. This can be plausibly accounted for by employing the microchannel flow model along with recently discovered changes in the glymphatic extracellular fluid channels during the sleep/wake cycle. These results suggest that the fluid

systems of the brain including the vascular, perivascular, and glymphatic systems, play a major role in setting the viscoelastic properties of regions of the brain. The implications for clinical medicine are that regulation and dysregulation of the neurovascular system and the glymphatic system will influence the parameters measured during elastography scans, which are increasingly available in magnetic resonance, ultrasound, and optical scanning systems. In humans, these elastography measures are typically conducted with shear wave frequencies closer to the 50–100 Hz band, and the trends shown in figure 8 imply that proportional changes in SWS measured at 2 kHz will also be present at lower frequencies. More research is required to refine the parameters required for accurate modeling, and for quantifying the effect of other cofactors which may include changes in the parenchymal constituents and abnormal variations in vascular and cerebral spinal fluid pressures. With improvement of models and experimental procedures, the stiffness changes observed here between sleep and awake states can be applied to basic neuroscience questions regarding sleep/wake biomechanics in both mice and humans. The link between elastography measurements and the regulation (or dysregulation) of the vascular and glymphatic compartments creates a unique means to noninvasively assess these in clinical studies. Furthermore, with advances in MR elastography, some important clinical problems in both diagnostics and prognostics can be addressed by measuring these values, for example differentiating normal aging from pathological diseases such as Alzheimer's disease, or surveying the effects of therapy.

Acknowledgments

This work was supported by National Institutes of Health Grants F30AG069293 and R21AG070331. The authors thank Arlo Gow for his data mining and curve fitting of anatomical data. We are also grateful to Professor Douglas H Kelley for his insightful questions and comments.

Appendix A. The relaxation spectrum based on anatomical measures

A key concept in the microchannel flow model is the causal relationship between the fractal branching vasculature and fluid channels, and the relaxation spectrum $A(\tau)$ that characterizes the rheological response. In this appendix A, we derive an explicit dependence based on measures available from anatomical studies. We begin with an applied force F on an elastic element producing a uniaxial stress σ_x with N cylindrical fluid channels of radius r open to a free surface shown in figure A1. Following the derivations in section 2 and applying Poiseuille's law, each channel has an output flow Q of approximately $Q_n \cong \sigma_x \pi r_n^4 / \eta 8 L_n$ where r is the radius of the microvessel, η is the viscosity of the fluid, L_n is the length of the vessel segment, and $L_n < L_0$, the length of the elastic element.

The loss of fluid volume during an incremental stress relaxation test is approximately $N \cdot Q$ and outflow will diminish the height of the block under compression. Assuming negligible change in cross section A, the volume change from the loss of fluid from the sample must be accounted for by a decrease in the x-dimension, or strain ε. Thus,

$$\frac{d\varepsilon_x}{dt} = \frac{N \cdot Q}{\mathrm{Vol}} = \frac{\sigma_x \pi N r^4}{\eta 8 L_n \mathrm{Vol}} \tag{13}$$

or

$$\sigma_x = \eta \left(\frac{8 L_n \mathrm{Vol}}{\pi N r^4} \right) \frac{d\varepsilon_x}{dt}, \tag{14}$$

where Vol is the volume of the cube in figure A1, and this stress–strain relationship resembles the simple dashpot where simple viscosity is replaced by the combination of factors in equation (14). By adding the elastic and fluid outflow strains we obtain the classical Maxwell model comprised of a series spring and dashpot, therefore the stress relaxation (SR) curve is a simple exponential decay. If $\varepsilon(r) = \varepsilon_0 U(t)$, where $U(t)$ is the unit step function, then

$$\sigma_{SR}(t) = \varepsilon_0 E \mathrm{e}^{-t/\tau} \text{ for } t \geqslant 0, \tag{15}$$

where the time constant τ is:

$$\tau = \frac{\eta 8 L_n \mathrm{Vol}}{E \pi N r^4}. \tag{16}$$

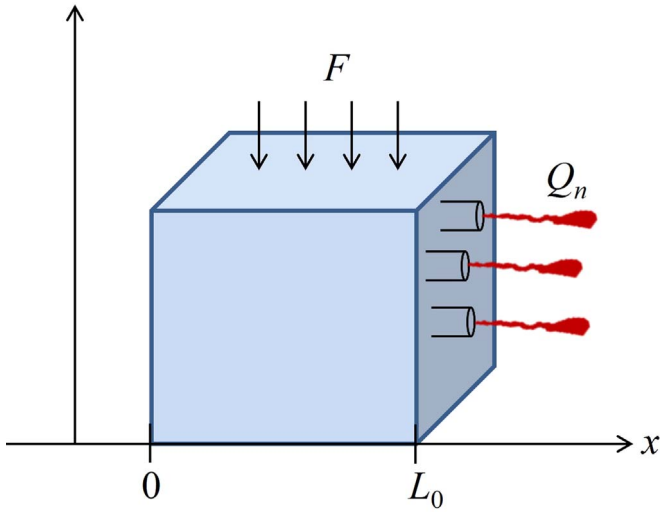

Figure A1. An elastic solid with multiple fluid-filled vessels subjected to uniaxial stress. This biphasic model has characteristic time constants dependent on the number and radii of the vessels.

We rewrite the time constant τ as:

$$\tau = \left(\frac{8\eta}{\pi E}\right)\left(\frac{L}{r}\right)\left(\frac{\text{Vol}}{f \cdot N}\right)\left(\frac{1}{r^3}\right), \tag{17}$$

where in a fractal branching network L and N are power law functions of r. Specifically, $L(r)/r$ represents the ratio of length to radius of vessels and $N(r)/\text{Vol}$ is the number density of vessels as a function of radius, and these are power laws that can be determined from anatomical studies. The tabulated data of Huang *et al* (1996) and several others are listed in table A1.

Using this data as a guideline for the brain parameters, we assume that:

$$\frac{N(r)}{\text{Vol}} \cong \frac{N_0}{r^{2.5}}, \tag{18}$$

or more generally,

$$\frac{N(r)}{\text{Vol}} = \frac{N_0}{r^d}, \tag{19}$$

where d is the power law exponent from anatomical studies.

One additional adjustment must be made to $N(r)/\text{Vol}$, however, in the stress relaxation configuration of figure A1. Flow Q can only be output at the free surface, and for small vessels and microchannels, only a fraction $f < 1$ of these will be intersecting with a free surface. Considering uniform distribution over the volume, the probability of a randomly positioned cylinder intersecting a free outer surface scales with length, $f \cong (L/L_{\text{max}})$, where L_{max} is the largest vessel in the ensemble. Thus, collecting all anatomical power laws in equation (17), we have

$$\begin{aligned}\tau(r) &= \left(\frac{8\eta}{\pi E N_0}\right)(r^{-(4-d)}) \\ &\cong \left(\frac{8\eta}{\pi E N_0}\right)(r^{-1.5})\end{aligned} \tag{20}$$

when d is taken at 2.5. This sets the relationship between time constants τ and vessel radii r within the ensemble, and replaces the earlier consideration of r^{-4} based on a single element and simply applying Poiseuille's Law (Parker 2014). To define the relaxation spectrum $A(\tau)$ we proceed in a similar manner. We postulate that the relaxation spectrum is defined by the arrangement and number density of channels as shown in figures 4(a)–(d) multiplied by the cross-sectional area of fluid channels incident on the free surface of figure A1. Thus, we write:

$$A(\tau) \propto A(r) \propto (r^2 \cdot N(r)) \propto \frac{r^2 N_0}{r^d} \propto \frac{N_0}{r^{d-2}}, \tag{21}$$

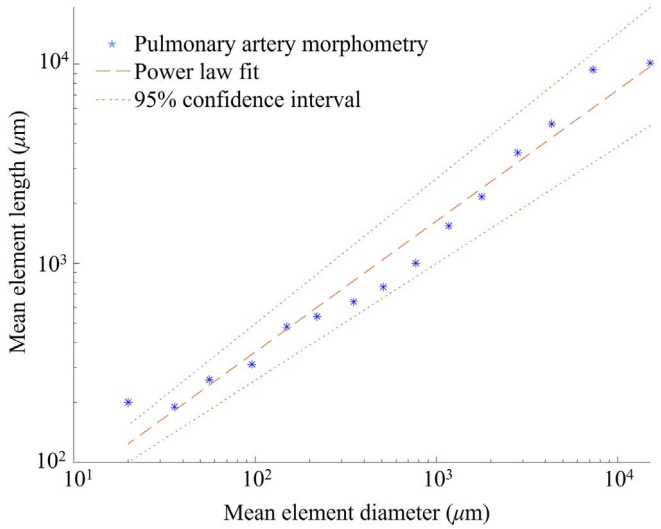

Figure A2. Power law relationship between element diameter and length in pulmonary arteries. Power law fit $d = 0.7 \pm 0.07$. Data are extracted from tabulations reported in Huang *et al* (1996).

and again applying the transformation rule:

$$A(\tau) = \frac{A(r)}{\left|\frac{d\tau}{dr}\right|}, \tag{22}$$

where $\tau = C/r^{4-d}$. Then we find:

$$A(\tau) = A_0\left(\frac{1}{\tau}\right)^{(7-2d)/(4-d)}. \tag{23}$$

With reference to table A1 again, and assuming $d = 2.5$, then

$$A(\tau) = \left(\frac{A_0}{\tau}\right)^{4/3}, \tag{24}$$

or $b = 1.33, a = 0.33$. This power law relaxation function sets $E(\omega) \cong |\omega|^{0.3}$ and $C(\omega) \cong |\omega|^{0.15}$ from the dispersion relations, commensurate with frequency-dependent parameters measured in soft tissues (Zhang *et al* 2007, Parker *et al* 2019).

Finally, as a first order approximation, we assume the following parameters for the model of the brain: $E = 1$ kPa (soft tissue range for the 'elastic' parenchyma), blood and extracellular fluid $\eta = 1.5 \times 10^{-3}$ Pa-s, and power laws shown in figures 4(b) and A2 extracted from the painstaking study of pulmonary vasculature of (Huang *et al* 1996), where we assume that Vol of the whole lung was 3 l or 3×10^6 mm^3. Inserting these particular values into the derivation of τ produces an estimate of $\tau = 0.006/r^{1.5}$ in units of seconds and r measured in mm. Thus, in our model of the brain, vessels of radius 1 mm would contribute to the relaxation spectrum $A(r)$ in the range of 0.006 s, or rather quickly on the scale of typical stress relaxation experiments. On the other hand, capillaries approximately 4 microns in radius would contribute to the relaxation spectrum in the range of 24 s, and the AQP4 pores at 3 nm would contribute in the range of over 10^8 s. The latter effect is experienced in stress relaxation experiments as an essentially constant baseline over short measurement periods, similar to an elastic response. Thus, even the smallest scale of microchannels has an influence on the overall stiffness of tissues and is subject to the changes from dilation/constriction mechanisms as indicated in equations (26)–(32).

Appendix B. Mapping changes from r to τ to $A(\tau)$ to $\sigma_{SR}(t)$ under dilation or constriction of channels in the unconfined space

Given the framework of equations (4)–(10), we derive the new relaxation spectrum $A_2(\tau_2)$ if all the vessel radii are increased or decreased by a factor of $r_2 = \chi r$ where $\chi > 1$ represents dilation and $\chi < 1$ constriction. To derive the altered relaxation spectrum function we employ the transformation rule of distributions (Papoulis 1987). Given a monotonic distribution $A(r)$ and a transformation $\tau_2 = C/(\chi r)^{1.5} = \tau/\chi^{1.5}$, then the transformed density function $A_2(\tau_2)$ is given by:

Table A1. Anatomical power laws. $N(r)$ = number density, $L(r)$ = vessel length as a function of r.

Parameter	Power law exponent	Tissue	References
$N(r)$	−2.7	pulmonary	Huang *et al* (1996)
$N(r)$	−2.5	brain arterial	Mut *et al* (2014)
$N(r)$	−1.3	cortex terminal arterial	Cassot *et al* (2006)
$N(r)$	−3.0	Murray's Law	Sherman (1981)
$L(r)$	+0.7	pulmonary	Huang *et al* (1996)
$L(r)$	+1.3	cortex terminal arterial	Cassot *et al* (2006)
$L(r)$	+0.75 to + 1.2	fractal tree structures	Hughes (2015) Takahashi (2014)

$$A_2(\tau_2) = \frac{A(\tau)}{\left|\frac{d\tau_2}{d\tau}\right|}. \tag{25}$$

Applying this rule, with $A(\tau) = A_0/\tau^b$, then:

$$A_2(\tau_2) = \left(\frac{1}{\chi^{1.5a}}\right)\left(\frac{A_0}{\tau_2^b}\right), \tag{26}$$

and this relationship conserves the total area under the relaxation spectrum:

$$\int_{\tau_{\min}}^{\tau_{\max}} A(\tau)d\tau = \int_{\tau_{2\min}}^{\tau_{2\max}} A_2(\tau_2)d\tau_2, \tag{27}$$

where

$$\begin{aligned} \tau_{2_{\max}} &= C/(\chi r_{\min})^{1.5} = (1/\chi)^{1.5}\tau_{\max} \text{ and} \\ \tau_{2_{\min}} &= C/(\chi r_{\max})^{1.5} = (1/\chi)^{1.5}\tau_{\min}. \end{aligned} \tag{28}$$

Finally, we examine the simple case of dilation (or constriction) within an *unconfined tissue* such that the extra blood volume associated with enlarged blood vessels is simply added to the organ volume. Although the skull presents a fixed outer boundary and therefore there must be some reallocation between fluid compartments, the most direct rheological consequence of dilation is examined below.

We first assume a baseline power law distribution of vessels between $r_{\min}$ and $r_{\max}$ consistent with the stress relaxation spectrum shown in figure 4(d):

$$A(\tau) = \frac{A_0}{\tau^b}\begin{cases} \tau_{\min} \leqslant \tau \leqslant \tau_{\max} \\ \text{or} \\ \dfrac{C}{r_{\max}^{1.5}} \leqslant \tau \leqslant \dfrac{C}{r_{\min}^{1.5}}, \end{cases} \tag{29}$$

and where the resulting stress relaxation function is given by equation (9). Next, consider that all vessel radii are altered proportionally by χ, where $\chi = 1$ represents the baseline case and after dilation or constriction:

$$r_2 = \chi r\begin{cases} \chi > 1 \text{ implies dilation} \\ \chi < 1 \text{ implies constriction}. \end{cases} \tag{30}$$

Again, applying the transformation rule, the new stress relaxation spectrum is defined as $A_2(\tau_2)$ where $\tau_2 = C/(r_2)^{1.5} = C/(\chi r)^{1.5} = (1/\chi)^{1.5}\tau$, so $d\tau_2/d\tau = (1/\chi)^{1.5}$, and applying equations (25) and (26) we find:

$$\sigma_{SR2}(t) = \left(\frac{A_0}{\chi^{1.5a}}\right)\frac{(\Gamma[a,\, t/\tau_{2_{\max}}] - \Gamma[a,\, t/\tau_{2_{\min}}])}{t^a}, \tag{31}$$

where $\tau_{2_{\max}}$ and $\tau_{2_{\min}}$ are given by equation (28). Thus, equations (28) and (31) provide the transformation of elastic properties as a function of vascular changes proportional to χ, in an unconfined space. In many cases, the leading term of $1/\chi^{1.5a}$ is the dominant factor, showing a strong effect where small amounts of dilation create a softening of the tissue. This term directly affects the complex modulus, where after dilation of only the glymphatic system, equation (12) becomes:

$$E(\omega) = A_1(-I\omega)(\beta[(-I\omega\tau_{\min}),\, (1-a),\, 0] - \beta[(-I\omega\tau_{\max}),\, (1-a),\, 0]) + (A_2/(\tau_{\min}^{a_2}\chi^{1.5a}))(1/a_2) \tag{32}$$

and where the τ time constants have been modified by equation (28). Conversely, small amounts of constriction will generate a hardening of the tissue, as demonstrated in Parker *et al* (2016).

As an example, figure 4(g) shows a nominal case where the vessels change with 20% dilation ($\chi = 1.2$) and then 20% constriction ($\chi = 0.8$), and using baseline parameters found in table 1 of Parker (2017a). These model parameters are representative of other soft vascularized tissues, and a 20% vasodilation is consistent with cortical laser Doppler flowmetry during sensory stimulation (Malonek *et al* 1997).

ORCID iDs

Gary R Ge https://orcid.org/0000-0001-9765-8076
Maiken Nedergaard https://orcid.org/0000-0001-6502-6031
Jannick P Rolland https://orcid.org/0000-0003-2747-4022
Kevin J Parker https://orcid.org/0000-0002-6313-6605

References

Abramowitz M and Stegun I A 1964 *Handbook of Mathematical Functions with Formulas, Graphs, and Mathematical Tables* (Washington: U.S. Govt. Print. Off.)
Arani A, Manduca A, Ehman R L and Huston Iii J 2021 Harnessing brain waves: a review of brain magnetic resonance elastography for clinicians and scientists entering the field *Br. J. Radiol.* **94** 20200265
Audette M A, Miga M, Nemes J, Chinzei K and Peters T M 2007 A survey of biomechanical modeling of the brain for intra-surgical displacement estimation and medical simulation *Biomech. Syst. Technol.* **4** 83–112
Bigot M, Chauveau F, Beuf O and Lambert S A 2018 Magnetic resonance elastography of rodent brain *Front. Neurol.* **9** 1010
Biot M A 1941 General theory of three-dimensional consolidation *J. Appl. Phys.* **12** 155–64
Biot M A 1962 Mechanics of deformation and acoustic propagation in porous media *J. Appl. Phys.* **33** 1482–98
Budday S, Sommer G, Haybaeck J, Steinmann P, Holzapfel G A and Kuhl E 2017 Rheological characterization of human brain tissue *Acta Biomater.* **60** 315–29
Cassot F, Lauwers F, Fouard C, Prohaska S and Lauwers-Cances V 2006 A novel three-dimensional computer-assisted method for a quantitative study of microvascular networks of the human cerebral cortex *Microcirculation* **13** 1–18
Christensen R M 1969 Viscoelastic properties of heterogeneous media *J. Mech. Phys. Solids* **17** 23–41
Comellas E, Budday S, Pelteret J P, Holzapfel G A and Steinmann P 2020 Modeling the porous and viscous responses of human brain tissue behavior *Comput Method Appl. M* **369** 113128
Ferry J D 1970 *Viscoelastic Properties of Polymers, Chapter 1* (New York, NY: Wiley)
Fung Y C 1981 *Biomechanics: Mechanical Properties of Living Tissues, Chapter 2* (New York: Springer)
Ge G R, Tavakol B, Usher D B, Adler D C, Rolland J P and Parker K J 2022 Assessing corneal cross-linking with reverberant 3D optical coherence elastography *J. Biomed. Opt.* **27** 026003
Gerischer L M, Fehlner A, Kobe T, Prehn K, Antonenko D, Grittner U, Braun J, Sack I and Floel A 2018 Combining viscoelasticity, diffusivity and volume of the hippocampus for the diagnosis of Alzheimer's disease based on magnetic resonance imaging *Neuroimage Clin.* **18** 485–93
Guo J *et al* 2019 Brain maturation is associated with increasing tissue stiffness and decreasing tissue fluidity *Acta Biomater.* **99** 433–42
Hiscox L V, Johnson C L, Barnhill E, McGarry M D, Huston J, van Beek E J, Starr J M and Roberts N 2016 Magnetic resonance elastography (MRE) of the human brain: technique, findings and clinical applications *Phys. Med. Biol.* **61** R401–37
Hiscox L V, Johnson C L, McGarry M D J, Perrins M, Littlejohn A, van Beek E J R, Roberts N and Starr J M 2018 High-resolution magnetic resonance elastography reveals differences in subcortical gray matter viscoelasticity between young and healthy older adults *Neurobiol. Aging* **65** 158–67
Huang W, Yen R T, McLaurine M and Bledsoe G 1996 Morphometry of the human pulmonary vasculature *J. Appl. Physiol.* **81** 2123–33
Hughes A D 2015 Optimality, cost minimization and the design of arterial networks *Artery. Res.* **10** 1–10
Kamiya A and Takahashi T 2007 Quantitative assessments of morphological and functional properties of biological trees based on their fractal nature *J. Appl. Physiol.* **102** 2315–23
Kassab G S 2006 Scaling laws of vascular trees: of form and function American journal of physiology *Heart Circulatory Physiol.* **290** H894–903
Klatt D, Hamhaber U, Asbach P, Braun J and Sack I 2007 Noninvasive assessment of the rheological behavior of human organs using multifrequency MR elastography: a study of brain and liver viscoelasticity *Phys. Med. Biol.* **52** 7281–94
Konofagou E E, Harrigan T P, Ophir J and Krouskop T A 2001 Poroelastography: imaging the poroelastic properties of tissues *Ultrasound Med. Biol.* **27** 1387–97
Lakes R S 1999 *Viscoelastic Solids* (Boca Raton, FL: CRC Press LLC)
Liu Z and Bilston L 2000 On the viscoelastic character of liver tissue: experiments and modelling of the linear behaviour *Biorheology* **37** 191–201
Ma Q, Ries M, Decker Y, Müller A, Riner C, Bücker A, Fassbender K, Detmar M and Proulx S T 2019 Rapid lymphatic efflux limits cerebrospinal fluid flow to the brain *Acta Neuropathol.* **137** 151–65
Malonek D, Dirnagl U, Lindauer U, Yamada K, Kanno I and Grinvald A 1997 Vascular imprints of neuronal activity: relationships between the dynamics of cortical blood flow, oxygenation, and volume changes following sensory stimulation *Proc. Natl Acad. Sci. U S A* **94** 14826–31
Munder T, Pfeffer A, Schreyer S, Guo J, Braun J, Sack I, Steiner B and Klein C 2018 MR elastography detection of early viscoelastic response of the murine hippocampus to amyloid β accumulation and neuronal cell loss due to Alzheimer's disease *J. Magn. Reson. Imaging* **47** 105–14
Murphy M C, Huston J 3rd and Ehman R L 2019 MR elastography of the brain and its application in neurological diseases *Neuroimage* **187** 176–83
Mut F, Wright S, Ascoli G A and Cebral J R 2014 Morphometric, geographic, and territorial characterization of brain arterial trees *Int. J. Numer. Method. Biomed. Eng.* **30** 755–66
Nicholson C 2022 The secret world in the gaps between brain cells *Phys. Today* **75** 26–32

Ormachea J, Lavarello R J, McAleavey S A, Parker K J and Castaneda B 2016 Shear wave speed measurements using crawling wave sonoelastography and single tracking location shear wave elasticity imaging for tissue characterization *IEEE Trans. Ultrason. Ferroelectr. Freq. Control* **63** 1351–60
Ormachea J and Parker K J 2021 Reverberant shear wave phase gradients for elastography *Phys. Med. Biol.* **66** 175001
Ormachea J and Parker K J 2022 A preliminary study of liver fat quantification using reported ultrasound speed of sound and attenuation parameters *Ultrasound Med. Biol.* **48** 675–84
Papoulis A 1987 *The Fourier Integral and its Applications* (New York: McGraw-Hill)
Parker K J 2014 A microchannel flow model for soft tissue elasticity *Phys. Med. Biol.* **59** 4443–57
Parker K J 2015 Experimental evaluations of the microchannel flow model *Phys. Med. Biol.* **60** 4227–42
Parker K J 2017a Are rapid changes in brain elasticity possible? *Phys. Med. Biol.* **62** 7425–39
Parker K J 2017b The microchannel flow model under shear stress and higher frequencies *Phys. Med. Biol.* **62** N161–7
Parker K J 2022 Power laws prevail in medical ultrasound *Phys. Med. Biol.* **67** 09TR2
Parker K J, Ormachea J, McAleavey S A, Wood R W, Carroll-Nellenback J J and Miller R K 2016 Shear wave dispersion behaviors of soft, vascularized tissues from the microchannel flow model *Phys. Med. Biol.* **61** 4890–903
Parker K J, Ormachea J, Zvietcovich F and Castaneda B 2017 Reverberant shear wave fields and estimation of tissue properties *Phys. Med. Biol.* **62** 1046–61
Parker K J, Szabo T and Holm S 2019 Towards a consensus on rheological models for elastography in soft tissues *Phys. Med. Biol.* **64** 215012
Patz S *et al* 2019 Imaging localized neuronal activity at fast time scales through biomechanics *Sci. Adv.* **5** eaav3816
Poul S S, Ormachea J, Hollenbach S J and Parker K J 2020 Validations of the microchannel flow model for characterizing vascularized tissues *Fluids* **5** 228
Rasmussen M K, Mestre H and Nedergaard M 2022 Fluid transport in the brain *Physiol. Rev.* **102** 1025–151
Ray L A and Heys J J 2019 Fluid flow and mass transport in brain tissue *Fluids* **4** 196
Razavi M S, Shirani E and Kassab G S 2018 Scaling laws of flow rate, vessel blood volume, lengths, and transit times with number of capillaries *Front. Physiol.* **9** 581
Risser L, Plouraboue F, Steyer A, Cloetens P, Le Duc G and Fonta C 2007 From homogeneous to fractal normal and tumorous microvascular networks in the brain *J. Cerebr. Blood. F Met.* **27** 293–303
Schmitt J M and Kumar G 1996 Turbulent nature of refractive-index variations in biological tissue *Opt. Lett.* **21** 1310–2
Sherman T F 1981 On connecting large vessels to small. The meaning of Murray's law *J. Gen. Physiol.* **78** 431–53
Sutera S P 1993 The history of Poiseuille's law *Annu. Rev. Fluid Mech.* **25** 1–19
Takahashi T 2014 *Microcirculation in Fractal Branching Networks* (Tokyo: Springer)
Testu J, McGarry M D J, Dittmann F, Weaver J B, Paulsen K D, Sack I and Van Houten E E W 2017 Viscoelastic power law parameters of *in vivo* human brain estimated by MR elastography *J. Mech. Behav. Biomed. Mater.* **74** 333–41
Turner K L, Gheres K W, Proctor E A and Drew P J 2020 Neurovascular coupling and bilateral connectivity during NREM and REM sleep *Elife* **9** e62071
West G B, Brown J H and Enquist B J 1997 A general model for the origin of allometric scaling laws in biology *Science* **276** 122–6
Xie L *et al* 2013 Sleep drives metabolite clearance from the adult brain *Science* **342** 373–7
Zhang M, Castaneda B, Wu Z, Nigwekar P, Joseph J V, Rubens D J and Parker K J 2007 Congruence of imaging estimators and mechanical measurements of viscoelastic properties of soft tissues *Ultrasound Med. Biol.* **33** 1617–31
Zvietcovich F, Pongchalee P, Meemon P, Rolland J P and Parker K J 2019 Reverberant 3D optical coherence elastography maps the elasticity of individual corneal layers *Nat. Commun.* **10** 4895